Journal of
Composites Science

MDPI

Article

Drum Shell-Inspired Fractal Lightweight Microlattice Structures with Tailored Mechanical and Transport Properties

Zhenbang Lei [1], Xuerui Xia [1], Jianle Zhang [1], Luobin Hu [1], Xu Wang [2] and Lei Zhang [1,*]

[1] School of Advanced Manufacturing, Nanchang Universidty, Nanchang 330006, China
[2] State IJR Center of Aerospace Design and Additive Manufacturing, School of Mechanical Engineering, Northwestern Polytechnical University, Xi'an 710072, China; x.wang@nwpu.edu.cn
* Correspondence: zhangleizzz@ncu.edu.cn

Abstract

Inspired by the mechanical principles governing efficient impact load transmission and dissipation in drum shells, this study proposes a novel hierarchical microlattice design strategy that integrates bionic concepts with fractal geometry, aiming to develop multifunctional microlattice structures combining superior mechanical performance with favorable fluid transport characteristics. Based on the hexagonal crystal structure (HCS), first- and second-order fractal designs were introduced to construct microlattice architectures of varying topological complexities, designated as F-HCS (first-order fractal HCS) and T-HCS (second-order fractal HCS), respectively. Ti-6Al-4V alloy specimens were fabricated via laser powder bed fusion (LPBF), and their mechanical responses and permeability characteristics were systematically investigated through quasi-static compression experiments and computational fluid dynamics (CFD) simulations. The results demonstrate that the second-order fractal architecture effectively optimizes stress distribution at nodal regions; under identical strut diameter conditions, its elastic modulus, yield strength, and energy absorption capacity significantly surpass those of the control structure. Nevertheless, the enhancement in topological complexity, while improving mechanical properties, concurrently increases fluid flow resistance and reduces permeability. This study quantitatively elucidates the intrinsic trade-off between mechanical performance and fluid transport in microlattice design, providing a critical theoretical basis for the rational design of multifunctional microlattices in integrated load-bearing and mass-transfer applications.

Keywords: bio-inspired design; fractal microlattice; additive manufacturing; mechanical and fluid transport trade-off; microlattice metamaterials

Check for updates

Academic Editor:
Christian Mittelstedt

Received: 2 June 2026
Revised: 11 July 2026
Accepted: 13 July 2026
Published: 17 July 2026

Copyright: © 2026 by the authors. Licensee MDPI, Basel, Switzerland. This article is an open access article distributed under the terms and conditions of the Creative Commons Attribution (CC BY) license.

1. Introduction

Aerospace thermal protection [1–3], compact heat exchangers [4–6], and bone tissue engineering scaffolds [7–9] demand structural materials simultaneously possessing high stiffness, strength, and open interconnected porosity. However, dense materials or simple porous structures struggle to reconcile both requirements: stiffness increases with decreasing porosity, yet excessively low porosity blocks fluid channels. How to independently regulate mechanical and transport properties constitutes a critical challenge in lightweight structural design.

Microlattice structures concentrate material into microscopic struts and nodes, enabling high specific stiffness, specific strength, and specific energy absorption at extremely

low relative densities [10–15]. Additive manufacturing technologies such as laser powder bed fusion (LPBF) have enabled the fabrication of geometrically complex microlattices [16–21], transitioning them from conceptual designs to practical applications. Nevertheless, classical microlattice topologies characterized by uniform strut diameters exhibit mechanical responses strictly following the Gibson–Ashby scaling law: elastic modulus and yield strength increase with relative density in a power-law relationship [22–25]. Within this framework, relative density becomes the core variable simultaneously governing mechanical load-bearing and fluid transport—increasing density enhances load-bearing capacity yet inevitably reduces porosity and increases flow resistance. This reveals the inherent trade-off between mechanical and transport properties [26–28].

Nature provides abundant design prototypes for lightweight, high-strength structures [29–33]. Inspired by the hollow internode structure of bamboo, Ma et al. [34] integrated plate and hollow-truss designs, significantly improving the load-bearing capacity and material utilization efficiency of lattice structures. Sun et al. [35] extracted key connection features from the microstructure of pomelo peel, constructing bio-inspired lattices with negative Poisson's ratio properties, whose mechanical performance and specific energy absorption surpassed conventional body-centered-cubic topologies. Zhang et al. [36] drew inspiration from the bimodal pore structure of wood, achieving robust load-bearing under high-throughput water flow through a microlattice overlapping strategy for structural–functional integrated catalysts. These studies demonstrate that bio-inspired strategies can optimize structural responses without substantially increasing mass by redistributing material and reconstructing topological connectivity.

Current research on alleviating the inherent contradiction between mechanical and transport properties primarily encompasses three directions: gradient design [37–40], topological innovation [41–44], and fluid transport [45–50]. Maskery et al. [51] systematically compared strut variants with uniform structures, revealing that gradient specimens achieved approximately twice the energy absorption of uniform structures, with compression initiating layer-by-layer collapse from low-density layers, effectively delaying global failure. Regarding topological innovation, Zheng et al. [52] investigated the influence of relative density on four triply periodic minimal surface lattices, finding that the primitive type exhibited stretch-dominated behavior and thus the highest stiffness, while gyroid, diamond, and wrapped types all displayed bending-dominated deformation, providing a basis for directional performance regulation through topological selection. In fluid transport, Ali et al. [46] systematically compared permeability and wall shear stress between lattice-type and gyroid-type scaffolds based on Newtonian and non-Newtonian blood flow models, discovering that permeability under the non-Newtonian model was significantly lower than under the Newtonian model, while wall shear stress was nearly doubled, revealing the important influence of fluid constitutive behavior on transport performance. He et al. [53] further proposed a material–structure–function integrated additive manufacturing strategy, achieving unprecedented specific energy absorption and stable stress platforms through cross-scale synergy between microstructural organization and mesoscopic structural stress regulation. However, the aforementioned studies mostly examined mechanical or transport properties independently under variable relative density conditions, lacking quantitative investigations of the relationship between topological complexity and dual performance under manufacturing process constraints (fixed strut diameter). Therefore, clarifying the independent contributions of fractal hierarchy to mechanical enhancement and flow resistance under controlled strut diameter conditions is essential for establishing multifunctional microlattice design criteria [54].

This study draws core design inspiration from a unique bio-inspired prototype—the drum shell. Though artificially constructed, the drum shell's hoop-tension shell mechanism

shares its mechanical principles with natural tension-shell structures (e.g., eggshells, turtle shells): both convert concentrated loads into uniform membrane stresses through curved-surface geometry, achieving efficient load-bearing that dissipates maximum energy with minimal material. As an efficient hoop-tension shell, the drum shell's exceptional impact resistance originates from its ability to efficiently convert external impact loads into uniform hoop tension and dissipate energy along optimal paths. This macroscopic load-bearing and microscopic force-flow optimization principle aligns closely with the fractal geometry concept of self-similar structural response optimization across multiple scales.

Despite these advances, existing studies predominantly optimize either mechanical or transport properties independently, or rely on density variation as the sole tuning knob—thereby inherently coupling the two performances and precluding independent regulation. A topology-driven strategy that decouples mechanical load-bearing enhancement from open-channel permeability preservation, without resorting to density gradients, remains elusive. To address this gap, this study proposes a novel multilevel microlattice design strategy integrating drum shell mechanics with fractal geometry: based on the hexagonal crystal structure (HCS), first-order and second-order fractal designs are introduced to construct a microlattice series with varying topological complexities, designated as first-order fractal hexagonal crystal structure (F-HCS) and second-order fractal hexagonal crystal structure (T-HCS), respectively. Employing LPBF technology to fabricate Ti-6Al-4V alloy specimens, and through systematic quasi-static compression experiments and computational fluid dynamics simulations, this study aims to quantitatively reveal, under controlled strut diameter conditions, how increasing topological complexity independently influences mechanical properties and fluid permeation performance, and to systematically establish the intrinsic trade-off relationship between the two, thereby providing theoretical foundations and performance prediction frameworks for multifunctional microlattice structures oriented toward load-bearing and mass transfer integrated applications.

2. Materials and Methods

2.1. Sample Preparation

Ti-6Al-4V powder particles exhibit near-spherical morphology with smooth surfaces and excellent flowability. The particle size distribution ranges from 20.4 to 49.6 μm, with an average particle diameter of 30.0 μm, satisfying LPBF process requirements. An EOS system was employed for additive manufacturing, with a laser power of 100 W, scanning speed of 1400 mm/s, hatch spacing of 60 μm, and layer thickness of 20 μm. After fabrication, samples were separated from the substrate via wire electrical discharge machining and ultrasonically cleaned in anhydrous ethanol to remove residual powder. Three replicate specimens were prepared for each configuration, totaling 21 samples for quasi-static compression testing.

2.2. Morphological Analysis and Compression Testing

A tungsten filament scanning electron microscope (SEM; VEGA3, TESCAN, Brno, Czech Republic) was utilized for microstructural analysis of as-built surfaces and post-compression fracture interfaces, with an accelerating voltage of 20 kV and working distance of 10 mm. Prior to testing, LPBF-fabricated specimens were ultrasonically cleaned in ethanol to ensure imaging quality. In accordance with ISO 13314:2011 [55], uniaxial quasi-static compression was conducted using a Shimadzu AG-IC 100 kN universal testing machine (Shimadzu, Kyoto, Japan) at a loading rate of 1.0 mm/min under displacement control mode. Engineering stress was calculated as $\sigma = F/A_0$ and engineering strain as $\varepsilon = \Delta h/h_0$, where F is the applied load measured by the load cell, A_0 is the initial cross-sectional area, Δh is the crosshead displacement, and h_0 is the initial specimen height. Stress–strain curves were processed via least-squares fitting: the elastic modulus was determined from the slope

of the initial linear elastic segment (strain range 0.05–0.15%); yield strength was defined using the 0.2% offset method; and compressive strength was defined as the peak stress in the engineering stress–strain curve.

2.3. Finite Element Model

Geometric models of HCS, F-HCS, and T-HCS structures were established in SOLIDWORKS 2024 based on design parameters and imported into nTopology 2025 for mesh generation: the solid domain was discretized using tetrahedral elements with local refinement at strut nodes and fractal feature regions to accurately capture stress concentration; the fluid domain employed free tetrahedral meshes with local refinement at strut surfaces and narrow fractal channel regions to ensure computational accuracy of flow fields within fractal channels. Mechanical and flow simulations were completed on ABAQUS 2024 and COMSOL Multiphysics 2024 platforms, respectively. Mesh convergence was verified using T-0.350 as a representative case: the permeability variation among three mesh sets (13.14 million, 14.57 million, and 17.00 million elements) was below 0.2%, confirming mesh independence. The final calculations adopted the 14.57-million-element mesh with a maximum element size of 0.9 mm and a minimum element size of 0.08 mm.

2.3.1. Mechanical Compression

A compression simulation model was developed for Ti-6Al-4V microlattice structures to analyze stress distribution and failure characteristics. The Ti-6Al-4V material is modeled as an elastic-plastic solid using an elastic-perfectly plastic constitutive model. Model parameters were configured based on the quasi-static experiments of Thijs et al. [18]: density 4450 kg/m^3, elastic modulus 120 GPa, and Poisson's ratio 0.34; material failure was governed by an equivalent plastic strain threshold. When this threshold was exceeded, elements were progressively degraded to simulate fracture, as reflected in the stress contour evolution. Contact conditions employed a Coulomb friction model with a friction coefficient of 0.1, and strut self-contact was enabled. Simulations were conducted at ambient temperature, applying 8% compressive strain (corresponding to 0.96 mm axial displacement) under axial displacement control. In the FE simulations, stress was computed as the volume-averaged von Mises stress over the solid elements, and strain was defined as the nominal strain calculated from the applied axial displacement boundary condition. Boundary constraints were defined as follows: the top platen permitted only axial displacement, while the bottom base was fully fixed in all degrees of freedom.

2.3.2. Fluid Flow Simulation

The computational fluid dynamics model investigated fluid permeability characteristics and mass transport mechanisms in porous media. In the fluid domain, the solid microlattice structure is treated as a rigid, impermeable wall; only the fluid phase (water) is solved, with no solid material constitutive model required. Numerical simulations employed the incompressible Navier–Stokes equations as the core governing equations [56], with constitutive relations expressed as:

$$\rho\left(\frac{\partial v}{\partial t} + (v \cdot \nabla)v\right) = -\nabla P + \mu\nabla^2 v + f,\ \nabla \cdot v = 0 \quad (1)$$

where ρ denotes fluid density (kg/m^3), μ denotes dynamic viscosity (Pa·s), v denotes the velocity field (m/s), P denotes the pressure field (Pa); and f represents body forces (neglected in this study, f = 0). Boundary conditions were set as follows: the inlet was defined as a velocity inlet (v = 0.001 m/s), and the outlet was defined as a pressure outlet (relative pressure of 0); the fluid domain dimensions were at the unit cell scale (12.350 × 10.742 × 10.392 mm).

Based on the inlet velocity, characteristic length, and water properties, the Reynolds number was calculated as Re ≈ 0.35, confirming laminar flow conditions. To accurately characterize steady-state permeability, periodic boundary conditions were applied in the computational domain, thereby analyzing permeation behavior under fully developed flow conditions.

The fluid domain utilized water as the working medium. The inlet velocity was set to 0.001 m/s. The pressure gradient (i.e., pressure drop ΔP) was calculated from the pressure difference between inlet and outlet cross-sections.

$$\Delta P = P_{\text{in}} - P_{\text{out}} \tag{2}$$

Based on established theoretical transport models, structural transport efficiency was quantitatively evaluated through permeability analysis [57], expressed as:

$$k = \frac{v\mu}{\nabla p}, \ \nabla p = \frac{\Delta P}{H} \tag{3}$$

Material property modules were loaded with standard water parameters: density 103 kg/m^3, dynamic viscosity coefficient 1.01 × 10^{-3} Pa·s. H denotes the model height.

3. Results and Discussion

3.1. Structural Design of HCS

Inspired by the efficient transmission and dissipation of impact loads in African drum shells, this study proposes a multilevel microlattice design strategy integrating bio-inspired concepts with fractal geometry. As shown in Figure 1A,B, the drum shell, as a typical hoop-tension shell, derives its exceptional load-bearing capacity from efficiently converting external impacts into uniform hoop tension and transmitting and dissipating energy along optimal paths on the hyperbolic shell surface. This macroscopic load-bearing and microscopic force-flow optimization mechanism provides the core bio-inspired prototype for microlattice structural design.

As shown in Figure 1C, the left panel presents the classical hexagonal crystal structure (HCS) unit cell, whose uniform straight-strut topology constitutes the design starting point; the right panel presents the drum shell-inspired double-conical variable-cross-section strut unit cell, in which the hyperbolic shell surface feature of the drum shell is abstracted into variable-cross-section struts while maintaining the topological connectivity of the hexagonal lattice, constructing the fundamental bio-inspired microlattice. This design inherits the hoop force-flow transmission advantage of the drum shell: the double-conical struts form natural thickening at nodes, effectively increasing connection areas and providing a geometric foundation for mitigating stress concentration.

To further enhance load-bearing efficiency and optimize energy absorption, fractal geometry is introduced for multilevel topological refinement while maintaining macroscopic porosity and double-conical features. As shown in Figure 1D, by inserting a first-order internal support fractal structure within the base HCS unit cell, the first-order fractal hexagonal crystal structure (F-HCS) is obtained. This design adds internal load-transfer paths within the original lightweight framework, enabling external loads to be collaboratively distributed through primary struts and fractal substructures. On this basis, to more finely regulate local stress gradients, a second-order fractal design is implemented at the midpoints of F-HCS struts, yielding the second-order fractal hexagonal crystal structure (T-HCS) (Figure 1E). This hierarchical fractal strategy achieves multiscale optimization of force-flow paths through successive refinement of feature sizes, without substantially increasing structural mass. The fractal nature of this strategy lies in that substructures at each level form topological self-similarity with the parent structure through multi-branch connections at

nodes, enabling external loads to be distributed and transferred across different scales, thereby inheriting the core characteristic of fractal geometry: "local-global self-similarity". Figure 1F illustrates the periodic three-dimensional stacking morphologies of the three structures, whose open pore channels retain connected pathways for fluid transport.

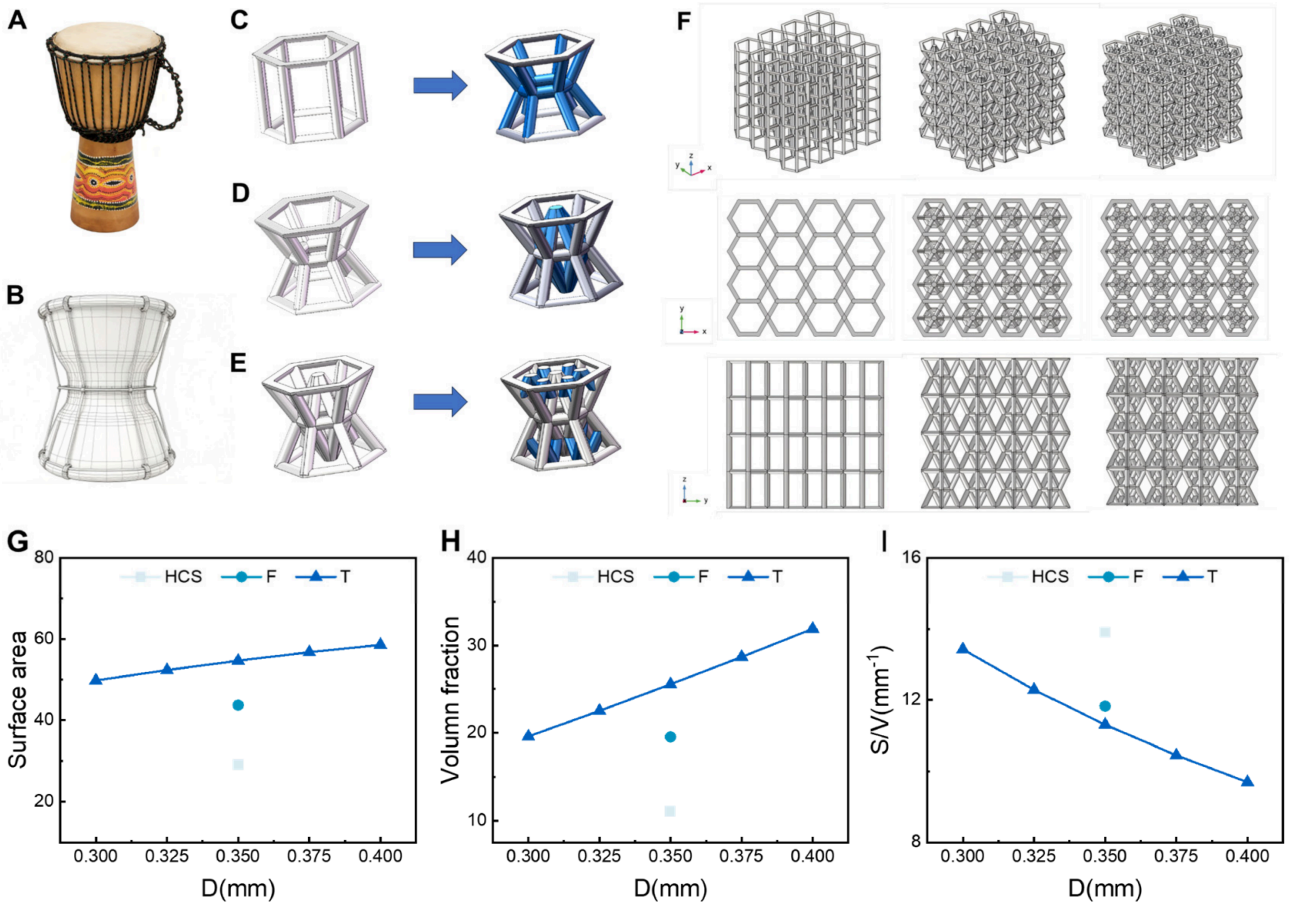


Figure 1. Drum shell-inspired fractal microlattice structural design and geometric parameter analysis: (**A**) African drum; (**B**) skeleton sketch of the drum; (**C**–**E**) CAD unit cell models of hexagonal crystal structure and drum shell-inspired lattice structures, corresponding to HCS, F-HCS, and T-HCS structures, respectively; (**F**) three-dimensional rendering of microlattice structures; (**G**) relationship between surface area and strut diameter; (**H**) relationship between relative density and strut diameter; (**I**) relationship between specific surface area and strut diameter.

To quantitatively characterize the influence of topological complexity on geometric parameters, HCS, F-HCS, and T-HCS are first compared laterally using a baseline strut diameter of 0.35 mm; on this basis, a parametric study of five strut diameters is further conducted for T-HCS to examine scale effects. As shown in Figure 1G–I, under the 0.35 mm baseline strut diameter, the relative density, total surface area, and specific surface area of the three structures exhibit significant differentiation dominated by topological complexity: with increasing fractal hierarchy, the solid volume fraction and total surface area increase under identical strut diameter, while specific surface area decreases. For T-HCS, as strut diameter increases, relative density exhibits a monotonically increasing trend (Figure 1H), total surface area increases correspondingly (Figure 1G), and specific surface area gradually decreases (Figure 1I). These results indicate that the introduction of fractal hierarchy not only alters local geometric morphology, but also, through the independent degree of freedom of strut diameter, achieves decoupled regulation of solid volume fraction and fluid

contact area while maintaining topological features, providing a structural foundation for subsequent coupled investigations of mechanical and transport properties.

3.2. Manufacturing Accuracy

All designed structures were fabricated via laser powder bed fusion (LPBF) using Ti-6Al-4V powder. Specimens were arranged as 4 × 4 × 4 cubic microlattices. This study employed T-HCS as the core variable, with strut diameter D varying from 0.300 mm to 0.400 mm in increments of 0.025 mm, designated as T-0.300, T-0.325, T-0.350, T-0.375, and T-0.400, respectively. Simultaneously, HCS and F-HCS with strut diameter D = 0.35 mm were prepared as controls, totaling seven independent sample groups.

Macroscopically, as shown in Figure 2B, the fabricated microlattice samples exhibit a typical uniform silver-gray metallic luster characteristic of Ti-6Al-4V alloy, with clearly visible overlapping melt pool morphologies. No obvious macroscopic pores or cracks were observed, indicating appropriate LPBF process parameter settings. Through measurement and calculation (Figure 2C), the measured mass of samples increases with structural density, ranging from 0.53 g (HCS) to 2.04 g (T-0.400). Analysis reveals that the measured mass (m) of all samples is slightly higher than their theoretical design values (m_d). This mass deviation (η_m) was quantified via Equation (4), with results indicating that mass deviation exhibits a negative correlation with structural relative density. This is primarily attributed to the fact that low relative density (high porosity) structures are more prone to generating support structures and powder adhesion during LPBF, leading to increased actual fabricated mass.

$$\eta_m = \left| \frac{m_d - m}{m} \right| \times 100\% \tag{4}$$

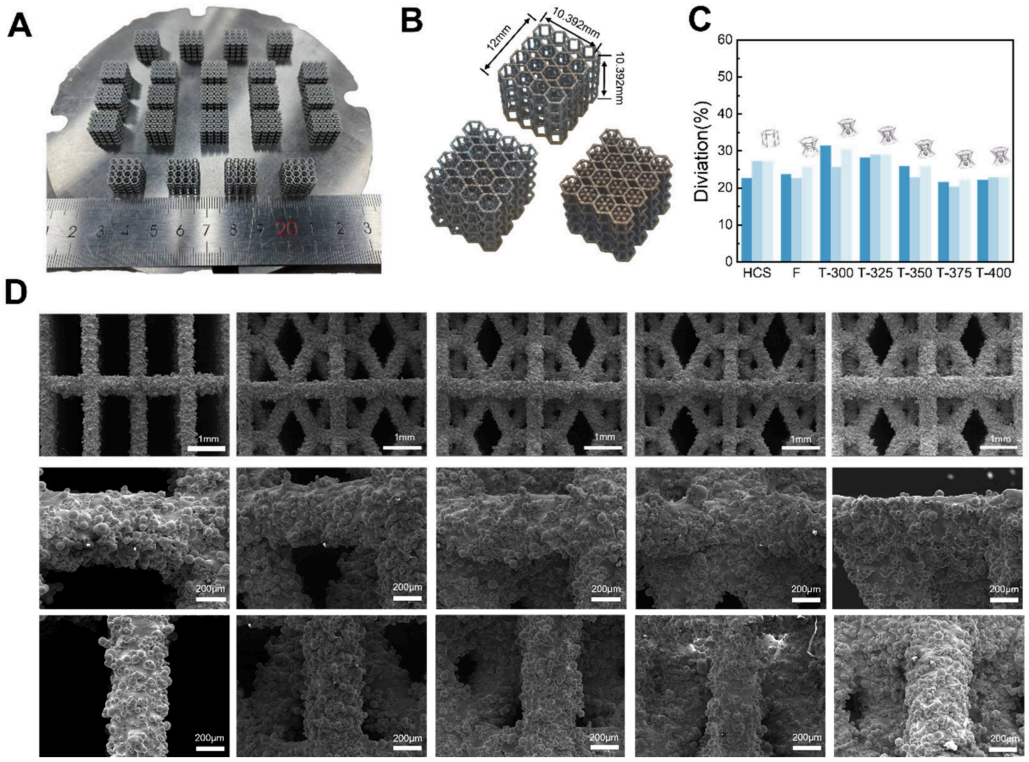


Figure 2. LPBF-fabricated Ti-6Al-4V microlattice structures and fabrication quality analysis: (**A**) seven sets of Ti-6Al-4V microlattice structures fabricated via LPBF; (**B**) designed three structural microlattices; (**C**) mass deviation plot of LPBF-fabricated samples versus theoretical values; (**D**) topological micrographs of HCS, F-0.35, T-0.35, T-0.30, and T-0.40 microlattices.

Scanning electron microscopy (SEM) observation of sample side morphologies enables direct verification of manufacturing geometric fidelity. Strut diameters were measured directly from SEM micrographs. As shown in Figure 2D, SEM images clearly demonstrate that the actual strut diameter of microlattices increases correspondingly with the designed D value, while pore sizes within the structures decrease accordingly, consistent with design expectations and proving the favorable formability of LPBF processes for such complex fractal microlattice structures. Further observation of the mesoscopic morphologies of different topologies reveals that the base HCS exhibits relatively smooth straight-strut surfaces with regular melt track textures aligned along the strut axis; the F-HCS diagonal strut surfaces exhibit slight staircase effects, yet overall geometric contours remain clearly defined; due to its highest topological complexity, the T-HCS exhibits localized powder sintering adhesion at the intersections of multilevel fractal substructures, with strut surface roughness slightly higher than the former two, but the geometric identifiability of fractal features remains satisfactory. The aforementioned mesoscopic morphological characteristics confirm the feasibility of LPBF fabrication of fractal hierarchical microlattice structures, with strut diameter deviations, surface roughness, and internal porosity all falling within typical ranges for LPBF Ti-6Al-4V microlattices (diameter deviation ±2–5%, Ra 5–15 μm, porosity <2%), providing a reliable sample foundation for subsequent mechanical and transport property testing.

3.3. Mechanical Response

3.3.1. Deformation Mechanism

Through uniaxial quasi-static compression experiments combined with synchronized imaging, the progressive failure processes of microlattice structures under different topological configurations and strut diameter parameters were systematically recorded. As shown in Figure 3, all specimens primarily exhibit elastic deformation and initial plastic buckling during the early compression stage (0–10% strain), with localized slender struts undergoing bending or fracture first due to stress concentration. As strain increases to approximately 20%, structures enter the progressive failure stage, yet failure modes exhibit significant differentiation among different topologies: the base HCS displays typical horizontal layer-by-layer collapse, with failure propagating downward layer-by-layer; whereas the F-HCS and T-HCS with introduced fractal topologies transition to shear band-dominated modes extending along approximately 45° diagonals. This topology-dependent transition from layer collapse to shear band failure originates from the reconstruction of nodal stress distribution by fractal design—multilevel fractal substructures disperse loads from nodes toward strut midsections, suppressing localized layer crushing and promoting collaborative deformation transfer over larger regions.

Further comparison of deformation behaviors among T-HCS series with different strut diameters reveals that the strut diameter parameter exerts significant regulation on failure localization degree. T-0.30 exhibits the most pronounced bending compliance during compression due to its highest strut slenderness ratio, with energy primarily dissipated through large-deflection bending of struts, leading to higher localization degree within shear band regions; whereas T-0.40 demonstrates enhanced strut bending stiffness and improved structural integrity due to increased strut diameter and relative density, with its failure evolving from localized shear toward global shear failure and more uniform progressive collapse. T-0.35 exhibits transitional characteristics between the two. This regularity indicates that, under fixed topological configuration, strut diameter as an independent geometric parameter can effectively regulate energy dissipation mechanisms and failure localization degree of structures.

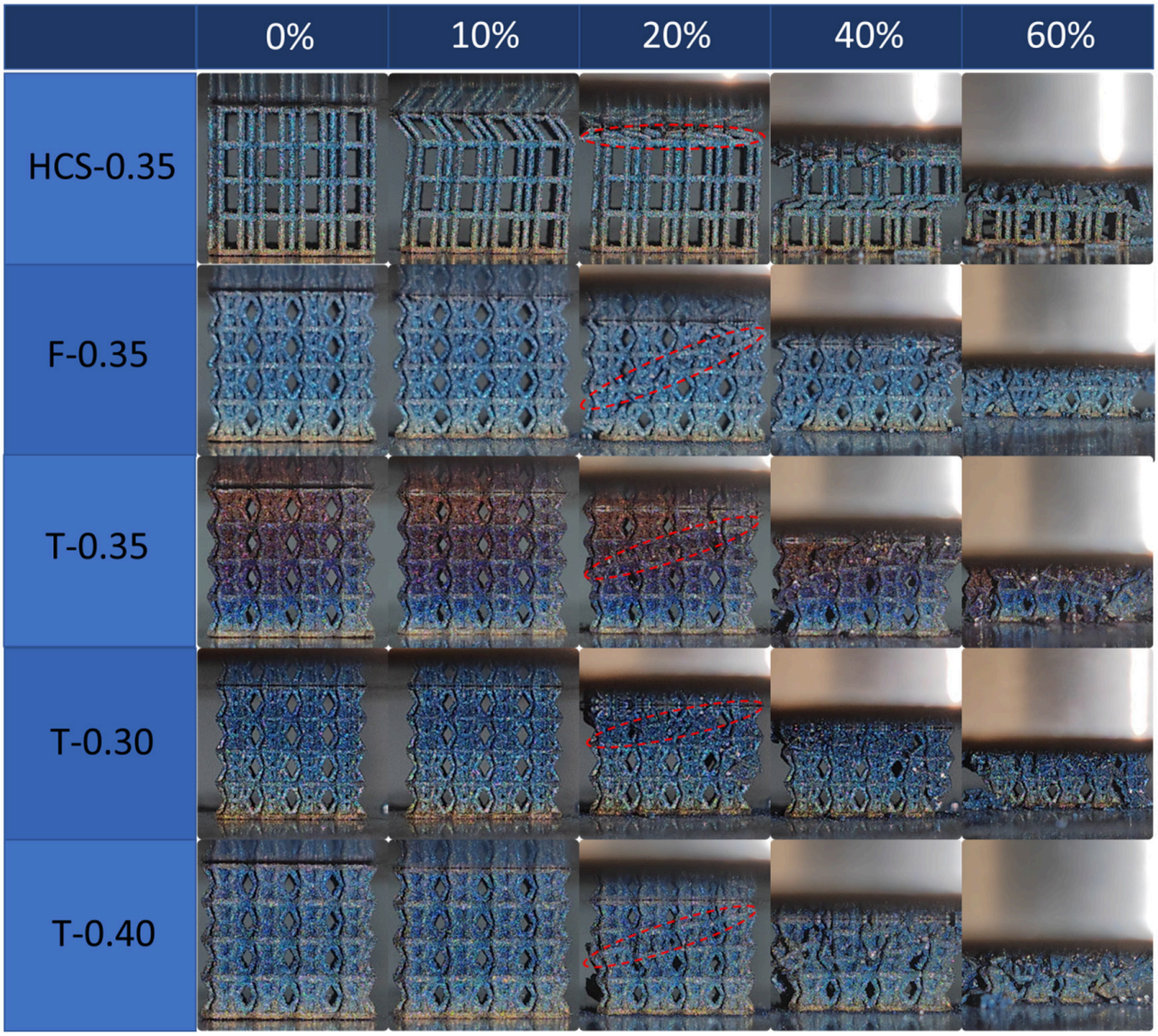


Figure 3. Quasi-static compression progressive deformation behaviors: deformation behaviors of HCS, F, T-0.35, T-0.30, and T-0.40 specimens at 10%, 20%, 40%, and 60% compressive strains. Red dashed ellipses indicate failure initiation and propagation: horizontal layer-by-layer collapse for HCS-0.35, and ~45° shear-band failure for F-HCS and T-HCS variants.

As strain continues to increase to 40–60%, all structures enter the densification stage, with original pores significantly compressed and struts undergoing large-area contact and overlap. Notably, post-compression fracture morphology analysis reveals that all specimen fracture surfaces exhibit distinct fibrous dimple characteristics, typical microscopic evidence of ductile fracture in Ti-6Al-4V alloy, indicating that crack propagation is closely related to microscopic plastic deformation, and structures maintain favorable plastic deformation capability rather than catastrophic brittle fracture during macroscopic failure. From the deformation mechanism perspective, HCS failure is characterized by bending-dominated layer-by-layer collapse, with stress concentration at nodes triggering local buckling that propagates sequentially through layers; F-HCS and T-HCS, however, transform into shear-dominated shear band failure due to the load-dispersing effect of fractal substructures on nodal loads, with deformation cooperativity significantly enhanced. This mechanism transition is consistent with the evolution of Mises stress from nodal concentration toward uniformization across fractal hierarchies observed in finite element results (Figure 5B), revealing the fundamental reason why fractal design optimizes mechanical properties.

3.3.2. Mechanical Properties

To systematically evaluate the influence of topological configuration on mechanical properties, HCS, F-HCS, and T-HCS structures were compared laterally using a baseline strut diameter of 0.35 mm. Figure 4A presents the typical compressive stress–strain curves of the three structures, all exhibiting the characteristic three-stage behavior of porous materials: initial linear elastic segment, plastic yield plateau segment, and densification segment. Notably, the first peak stress of T-0.35 is significantly higher than those of HCS and F-0.35, and stress fluctuations in the plateau region are more moderate after entering the plateau, indicating a transition from localized brittle fracture to progressive stable collapse. To quantitatively compare the energy absorption capability, the specific energy absorption (SEA) is defined as:

$$SEA = \frac{\int_0^{\varepsilon_d} \sigma d\varepsilon}{\rho} \quad (5)$$

where σ is the engineering stress, ε_d is the densification strain, and ρ is the apparent density of the microlattice structure. Figure 4C further confirms through specific energy absorption curves that T-0.35 accumulates significantly superior energy absorption values throughout the compression history compared to the other two.

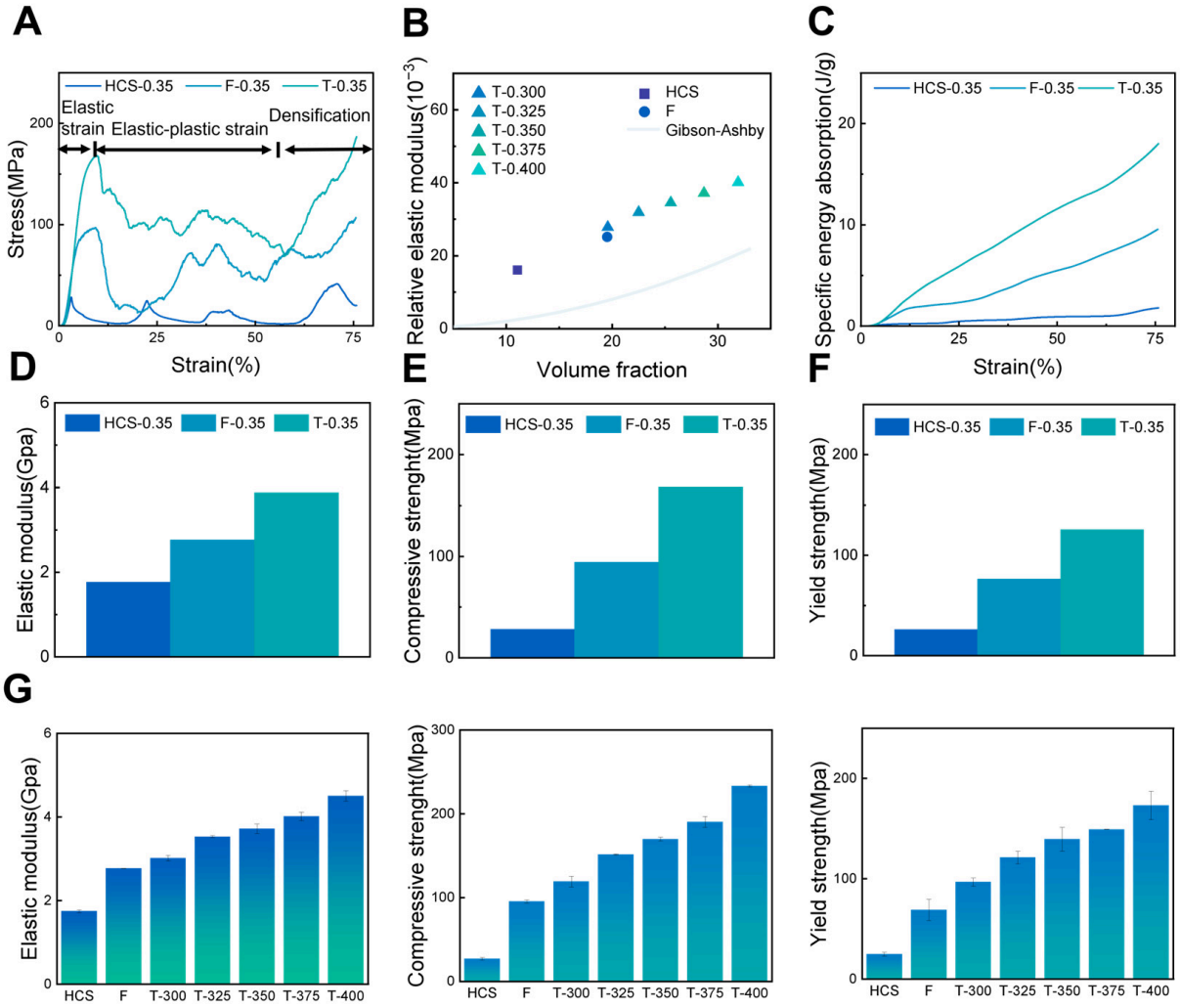


Figure 4. Influence of topological configuration on mechanical properties: (**A**) stress-strain curves of three models; (**B**) Ashby plot of relative elastic modulus versus volume fraction; (**C**) specific energy absorption; (**D**) elastic modulus; (**E**) compressive strength; (**F**) yield strength; (**G**) experimental error bars of seven sample groups.

Quantitative comparison of key mechanical parameters (Figure 4D–F) reveals that, under identical strut diameter constraints, the elastic modulus, yield strength (0.2% offset method), and compressive strength of T-0.35 structure comprehensively surpass those of F-0.35 and the base HCS. This topology-dependent enhancement effect indicates that the increase in fractal hierarchy itself can significantly improve mechanical properties, with the fundamental reason lying in that the second-order fractal design of T-HCS optimizes node connections, effectively mitigating stress concentration, thereby more fully exploiting the load-bearing potential of the material. To further exclude interference from relative density differences on performance comparisons, Figure 4B presents an Ashby plot of relative elastic modulus versus volume fraction, with results showing that the T-HCS series overall lies above the Gibson–Ashby scaling law, confirming that the mechanical enhancement from fractal design originates not merely from increased material volume but from topological optimization achieving redistribution of force-flow paths. Figure 4G further validates the reliability of the above conclusions through experimental error bar plots of seven sample groups, with small error ranges for each group indicating good experimental repeatability.

To validate experimental findings and reveal underlying deformation mechanisms, finite element models corresponding to experiments were established. Figure 5A superimposes the simulated and experimental stress–strain curves of HCS, F-0.35, and T-0.35 structures. Results indicate that the simulation models can satisfactorily capture the stiffness responses of the three structures in the elastic segment and overall stress levels in the plateau region, confirming the basic predictive capability of the models for macroscopic mechanical behavior trends; simultaneously, certain deviations exist between simulation and experiment in local peak stresses and fluctuation details, primarily originating from actual manufacturing defects (such as surface roughness, microporosity) and material constitutive simplifications. Based on this model, Figure 5B presents the Mises stress distribution evolution of the three structures at 0%, 10%, 20%, 40%, and 60% compressive strains. Clear observation reveals that the base HCS exhibits significant stress concentration at horizontal and vertical strut intersection nodes at 10% strain, with high-stress regions appearing as localized red hotspots, rapidly triggering strut fracture and layer-by-layer collapse with increasing strain; F-HCS disperses high-stress regions along diagonal struts through first-order fractal design, reducing stress peaks at nodes, yet primary node regions remain weak links, with shear bands initiating along diagonal directions visible at 20% strain; whereas the stress contour of T-0.35 structure demonstrates that second-order fractal substructures effectively channel concentrated loads at nodes into multilevel microscopic strut networks, with high-stress regions homogenizing along fractal hierarchies, and no catastrophic localized fracture occurring even at 40% strain, with significantly improved deformation coordination. This stress redistribution mechanism indicates that the multilevel fractal design of T-HCS is not simply increasing material usage, but rather achieving force-flow path redistribution through topological optimization, thereby enhancing load-bearing efficiency and failure stability without increasing structural mass, intuitively explaining the superiority of its experimental performance from the mechanical mechanism perspective.

On the basis of establishing T-HCS as the optimal topology, the refined regulation law of strut diameter parameters on mechanical properties of T-HCS series was further systematically investigated. Figure 6A presents the typical compression curves of T-HCS series (D = 0.300, 0.325, 0.350, 0.375, 0.400 mm). With increasing strut diameter, initial stiffness, peak stress, and plateau stress of structures all exhibit upward trends, yet the overall morphology of stress–strain curves remains similar, indicating that topological configuration has a decisive effect on deformation mode, while strut diameter primarily regulates load-bearing magnitude. Notably, curves of T-0.300 and T-0.325 rapidly drop

after the elastic segment and enter low-stress plateaus, reflecting load-bearing instability of slender struts under large-deflection bending; whereas curves of T-0.375 and T-0.400 maintain higher stress levels after reaching peaks, with reduced plateau fluctuation amplitudes, indicating that enhanced strut bending stiffness promotes structural transition from localized brittle fracture to progressive stable collapse.

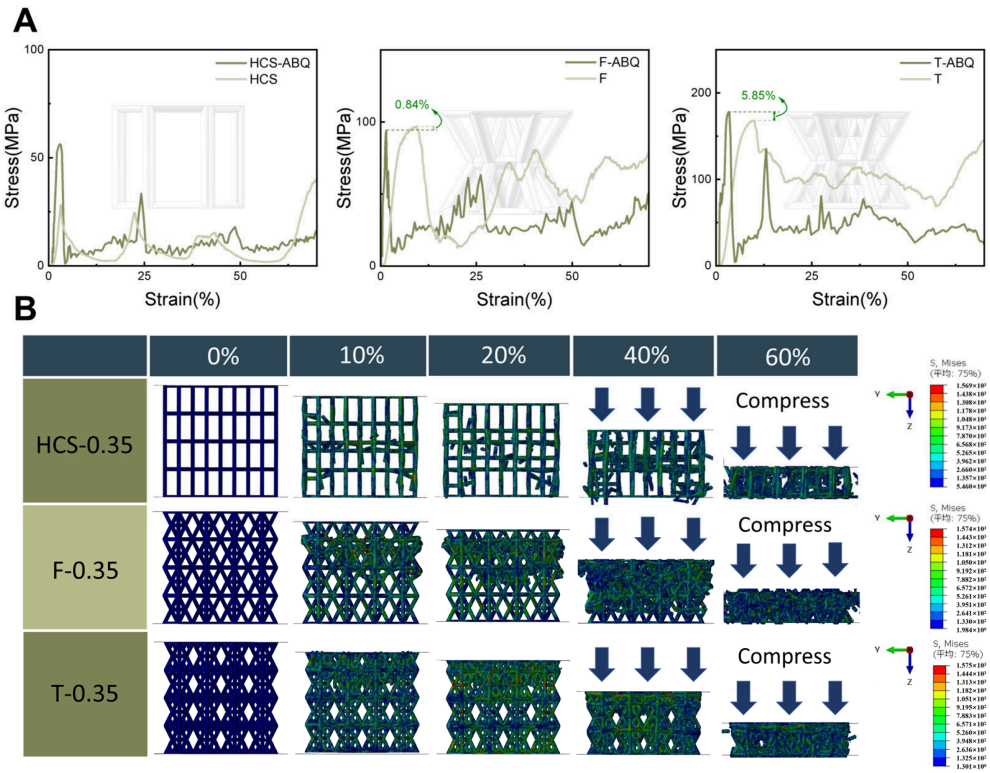


Figure 5. Compression finite element simulation validation: (**A**) simulated and experimental stress–strain curves of three models; (**B**) compression simulations of three models.

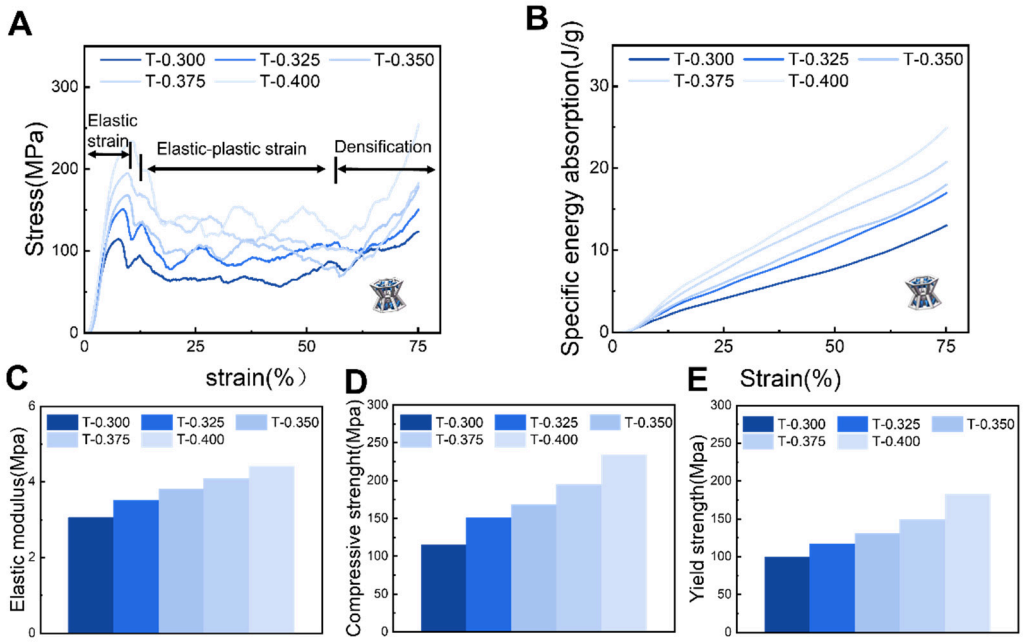


Figure 6. Parametric mechanical properties of T-HCS series strut diameters: (**A**) stress–strain curves of T-HCS; (**B**) specific energy absorption; (**C**–**E**) elastic modulus, compressive strength, and yield strength.

Figure 6B reveals that specific energy absorption increases approximately linearly with strut diameter. Quantitative statistics in Figure 6C–E further corroborate this regularity: elastic modulus, compressive strength, and yield strength all steadily increase with strut diameter, with no obvious performance saturation signs within the 0.300–0.400 mm range. This linear response relationship indicates that, within this strut diameter interval, mechanical properties of T-HCS are primarily dominated by solid volume fraction, and strut diameter as an independent geometric parameter can effectively and predictably regulate load-bearing capacity. However, excessively large strut diameters will significantly reduce structural porosity, which is unfavorable for multifunctional application scenarios requiring concurrent fluid transport. Comprehensively weighing absolute mechanical performance and pore connectivity requirements, the T-0.350 structure demonstrates relatively optimal comprehensive load-bearing efficiency within the parameter range of this study.

Experimental and simulation results jointly demonstrate that: (1) through introducing second-order fractal T-HCS topology, stress distribution can be effectively improved, with mechanical properties significantly surpassing traditional HCS and first-order fractal F-HCS structures; (2) for T-HCS series, mechanical properties and specific energy absorption increase approximately linearly with strut diameter, with T-0.350 achieving relatively optimal balance between load-bearing efficiency and porosity. The above findings provide quantitative foundations for high-performance lightweight microlattice structural design oriented toward load-bearing and mass transfer integrated applications.

3.3.3. Fluid Transport Properties

To comprehensively evaluate the multifunctional potential of the designed fractal microlattice structures, this study further systematically analyzes permeability and internal flow field characteristics through computational fluid dynamics (CFD) simulations, aiming to reveal the influence of structural topology on fluid transport efficiency.

Figure 7A presents a schematic diagram of the periodic flow channel computational model established in COMSOL Multiphysics. This model employs water as the working medium, with constant inlet velocity applied, and calculates pressure drop and flow field distribution as fluid passes through porous structures by solving steady-state incompressible Navier–Stokes equations (Equation (1)). Structural permeability (k) is calculated from inlet–outlet pressure drop (ΔP) according to Darcy's law (Equation (3)), serving as the core metric for quantifying fluid passage capability.

Figure 7B compares simulated and experimental permeabilities of HCS, F-0.35, and T-0.35 structures. Experimental data clearly demonstrate that, under identical strut diameter (D = 0.35 mm), permeabilities of the three structures exhibit a definitive monotonically decreasing trend: HCS possesses the highest permeability (~22×10^{-9} m^2), F-HCS is intermediate (~15×10^{-9} m^2), and T-0.35 is the lowest (~13×10^{-9} m^2). This ranking aligns with physical intuition: the straight-channel structure of HCS is the most unobstructed, while the introduction of fractal hierarchy increases flow channel tortuosity and surface friction, leading to progressively increased flow resistance. Simulation results after mesh convergence verification show good consistency with experimental data, similarly reflecting the permeability degradation pattern with increasing fractal hierarchy, validating the reliability of the CFD model in capturing the influence of topological complexity on fluid resistance.

Figure 7C further presents the dynamic trend of permeability with inlet velocity variation. For HCS, F-HCS, and T-HCS topological structures, permeability all exhibits a decreasing trend with increasing inlet velocity, consistent with non-Darcy flow characteristics in porous media. Notably, with increasing fractal hierarchy, permeability curves progressively shift downward: T-HCS consistently remains at the lowest position, F-HCS is

intermediate, and HCS is the highest; simultaneously, the decreasing magnitudes of F-HCS and T-HCS curves with velocity increase are more moderate compared to HCS, with T-HCS being particularly stable, indicating that more complex flow channel structures exhibit lower sensitivity to velocity variations and more stable flow behavior. In contrast, although HCS structure possesses higher permeability, its decreasing curve is the steepest. This figure corroborates from a dynamic dimension that topological structure is the fundamental factor determining transport performance.

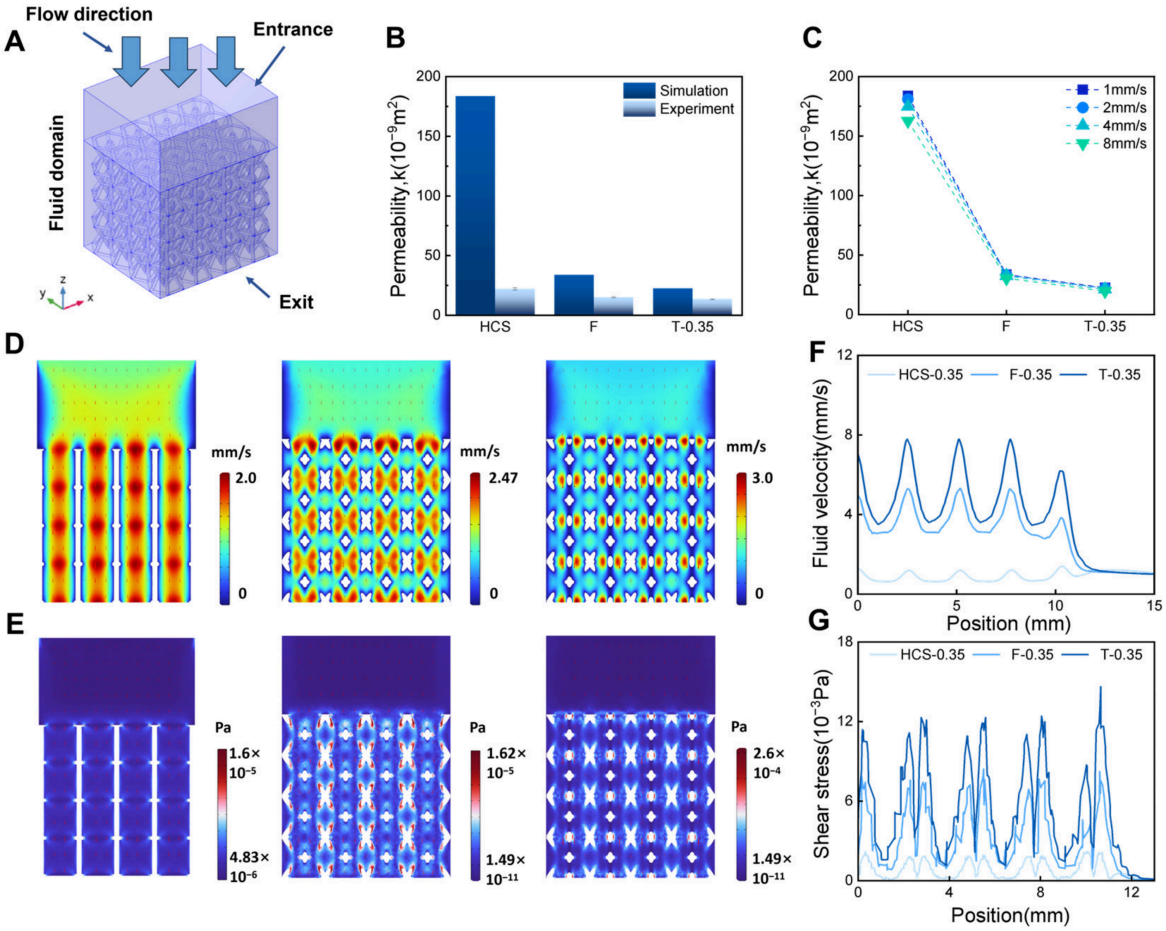


Figure 7. Numerical simulation analysis of fluid transport properties: (**A**) COMSOL model schematic; (**B**) permeability comparison of simulation and experiment for three models; (**C**) permeability variation trend with flow velocity; (**D**) velocity contour plots of three models; (**E**) pressure contour plots of three models; (**F**) velocity line plots; (**G**) pressure line plots.

Figure 7D,E visualize field distributions of fluid flowing through central cross-sections of the three structures in the form of velocity contour plots and pressure contour plots, respectively. From the velocity contour plots in Figure 7D, it can be observed that in the HCS structure, high-velocity flow regions (red) concentrate in the centers of wide channels between struts, with relatively uniform flow field distribution. In F-HCS and T-HCS structures, due to interference from fractal struts, high-velocity flow regions are segmented and compressed, with fluid accelerating through narrower gaps more frequently, while more pronounced low-velocity wake regions (blue) form behind struts. Corresponding pressure contour plots in Figure 7E reveal that pressure gradients (color variations) are not uniformly distributed within structures, with higher pressures in flow channel contraction regions and strut upstream faces, and lower pressures in expansion regions and downstream faces. The T-HCS structure exhibits the most dramatic internal pressure field variations due to its most complex geometry.

To quantitatively compare field variable variations along the flow direction, Figure 7F,G extract velocity and pressure distribution curves along the flow channel centerline. The velocity line plot in Figure 7F further confirms that velocity fluctuations along the centerline of the T-HCS structure are the most frequent with the largest amplitude variations, indicating that fluid undergoes more frequent acceleration and deceleration processes within this structure. The pressure line plot in Figure 7G demonstrates that wall shear stress along the flow path of the T-HCS structure is significantly higher than the other two, corroborating the conclusion of its minimum permeability in Figure 7B—greater flow resistance implies larger pressure differences required to drive identical flow rates, yet multilevel fractal substructures simultaneously provide larger fluid–solid contact areas.

Comprehensive analysis reveals that fractal design significantly enhances microlattice structural mechanical properties while inevitably increasing fluid flow resistance, leading to reduced permeability. This trade-off relationship between mechanical and permeation performance provides critical foundations for microlattice structural design oriented toward multiphysics applications (such as implants with combined load-bearing and heat dissipation/filtration functions, catalyst supports, or heat exchangers). In practical applications, topology selection among HCS, F-HCS, and T-HCS can be made according to dominant requirements (e.g., higher strength or higher permeability).

3.3.4. Mechanical–Transport Coupling Analysis

The multifunctional design of microlattice structures essentially represents synergistic regulation of multi-physics performance including mechanical load-bearing and fluid transport. The preceding sections respectively revealed the independent influences of topological complexity and strut diameter on individual properties, yet a unified design framework for quantitatively describing the synergistic evolution of multiple properties with geometric parameters remains to be established. To this end, a mechanical–transport performance correlation map based on the T-HCS series is constructed (Figure 8), systematically investigating the synergistic regulation mechanism of strut diameter on mechanical and transport properties under fixed topology.

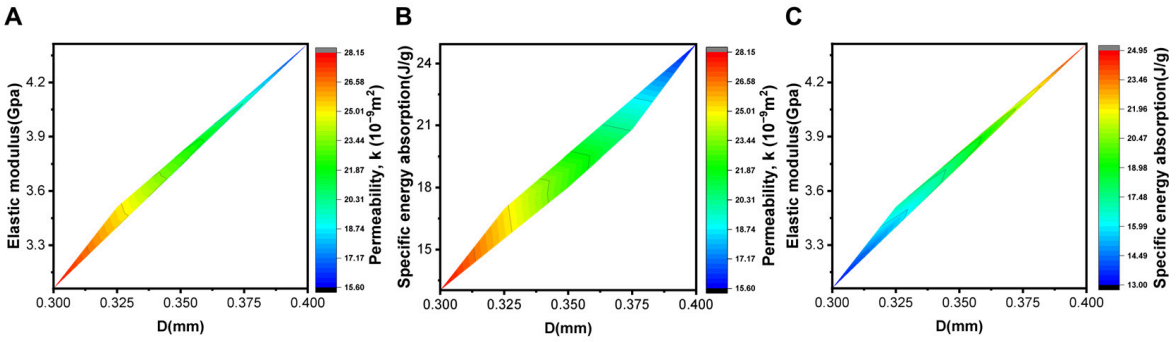


Figure 8. Mechanical-transport coupling performance analysis of T-HCS series: (**A**) elastic modulus-permeability; (**B**) specific energy absorption-permeability; (**C**) elastic modulus-specific energy absorption.

Figure 8A,B respectively present the synergistic evolution laws of elastic modulus, specific energy absorption, and permeability. As D increases from 0.300 mm to 0.400 mm, elastic modulus rises from approximately 3.0 GPa to 4.3 GPa, specific energy absorption synchronously increases monotonically, while permeability decreases from 28.15×10^{-9} m^2 to 15.60×10^{-9} m^2. This regularity indicates that increasing strut diameter simultaneously enhances structural load-bearing capacity by increasing solid volume fraction, yet simultaneously compresses effective cross-sectional areas of fluid channels and increases wall friction, thereby significantly increasing flow resistance. Figure 8C further reveals the synergistic growth trend of elastic modulus and specific energy absorption

with increasing D. Within the T-HCS topological framework, elastic modulus and specific energy absorption can be synchronously enhanced through the same geometric parameter, exhibiting an internal synergistic enhancement effect of mechanical properties; however, this synergistic optimization of mechanical properties is always achieved at the expense of permeability, reflecting the inherent trade-off mechanism among multiple properties.

The above results demonstrate that strut diameter D is a critical variable for synergistically regulating mechanical and fluid transport properties. Through precise regulation of D, directional trade-offs between load-bearing capacity and transport efficiency can be achieved: decreasing D favors obtaining high permeability, applicable to mass transfer-dominated scenarios; increasing D can significantly enhance elastic modulus and specific energy absorption, applicable to load-bearing-dominated scenarios. The T-0.350 structure exhibits relatively optimal comprehensive performance among elastic modulus, specific energy absorption, and permeability within the parameter range of this study, providing quantified synergistic regulation foundations for multifunctional microlattice structures oriented toward load-bearing and mass transfer integrated applications.

4. Conclusions

This study integrates bionics and fractal geometry to design and fabricate novel multilevel fractal microlattice structures (T-HCS), and systematically characterizes their quasi-static compression mechanical properties and fluid transport characteristics. The main conclusions are as follows: (1) Under identical strut diameter conditions, T-HCS effectively optimizes nodal force-flow transmission paths through second-order fractal design, mitigating stress concentration, with its elastic modulus, yield strength, and specific energy absorption significantly surpassing those of F-HCS and HCS; (2) T-HCS mechanical properties increase approximately linearly with strut diameter, yet porosity synchronously decreases, exerting adverse effects on fluid transport, with the T-0.350 structure achieving a relatively optimal balance between load-bearing efficiency and porosity within the parameter range of this study; (3) Increasing fractal hierarchy and strut diameter simultaneously enhance mechanical properties while weakening fluid transport, with T-HCS exhibiting the highest flow resistance and lowest permeability due to its complex tortuous flow channels, whereas HCS possesses optimal permeation performance, revealing the inherent trade-off relationship between mechanical and fluid transport properties.

The above findings provide theoretical foundations and design guidance for multifunctional microlattice structures oriented toward load-bearing and mass transfer integrated applications. Future work may further explore gradient fractal designs for spatial regulation of performance trade-offs, and extend to complex service environments such as dynamic impact, fatigue, and fluid–structure coupling.

Author Contributions: Conceptualization, X.X.; Methodology, X.X. and X.W.; Software, X.W.; Validation, X.X.; Investigation, J.Z.; Resources, J.Z. and L.Z.; Writing—original draft, Z.L.; Writing—review & editing, Z.L.; Visualization, J.Z. and L.H.; Supervision, L.H. and L.Z.; Project administration, L.H. and L.Z.; Funding acquisition, L.Z. All authors have read and agreed to the published version of the manuscript.

Funding: This research was funded by the National Key Research and Development Program of China (grant numbers 2024YFF0505001), the Natural and Science Foundation of China (Grant No. 52305360), the Key R&D Program of Jiangxi Province, China (No. 20252BCE310033), and the GanPo Talent Plan of Jiangxi Province (No. gpyc20240039).

Data Availability Statement: The original contributions presented in this study are included in the article. Further inquiries can be directed to the corresponding author.

Acknowledgments: This work was sponsored by the National Key Research and Development Program of China (grant numbers 2024YFF0505001), the Natural and Science Foundation of China (Grant No. 52305360), the Key R&D Program of Jiangxi Province, China (No. 20252BCE310033), and the GanPo Talent Plan of Jiangxi Province (No. gpyc20240039).

Conflicts of Interest: The authors declare no conflict of interest.

References

1. Gu, D.; Shi, X.; Poprawe, R.; Bourell, D.L.; Setchi, R.; Zhu, J. Material-structure-performance integrated laser-metal additive manufacturing. *Science* **2021**, *372*, eabg1487. [CrossRef] [PubMed]
2. Khan, M.H.; Li, B.; Tan, K.T. Impact Performance and Bending Behavior of Carbon-Fiber Foam-Core Sandwich Composite Structures in Cold Arctic Temperature. *J. Compos. Sci.* **2020**, *4*, 133. [CrossRef]
3. Zhao, H.; Liao, Q.; Li, Y.; Chu, X.; Yuan, S.; Qin, L. Additive Manufacturing of Silicon Carbide Microwave-Absorbing Metamaterials. *Addit. Manuf. Front.* **2025**, *4*, 200186. [CrossRef]
4. Maconachie, T.; Leary, M.; Lozanovski, B.; Zhang, X.; Qian, M.; Faruque, O.; Brandt, M. SLM lattice structures: Properties, performance, applications and challenges. *Mater. Des.* **2019**, *183*, 108137. [CrossRef]
5. Wang, L.; Tong, Z.; Song, F.; Yin, W.; Wang, L.; Miao, K.; Li, D. Controllable Energy Absorption Design and 3D Printing of High Energy Absorbing Biomimetic Double-Layer Impact-Resistant Structure. *Addit. Manuf. Front.* **2025**, *4*, 200193. [CrossRef]
6. Zhou, D.; Yan, K.; Du, Q.; Zhang, C.; Liu, T.; Xie, T.; Qin, S.; Qiao, H.; Sun, L.; Xu, J. Review of mechanical performance and structural integrity challenges of AM materials and components in nuclear reactors. *Addit. Manuf. Front.* **2025**, *4*, 200271. [CrossRef]
7. Wang, Y.; Zhang, L.; Daynes, S.; Zhang, H.; Feih, S.; Wang, M.Y. Design of graded lattice structure with optimized mesostructures for additive manufacturing. *Mater. Des.* **2018**, *142*, 114–123. [CrossRef]
8. Zheng, X.; Smith, W.; Jackson, J.; Moran, B.; Cui, H.; Chen, D.; Ye, J.; Fang, N.; Rodriguez, N.; Weisgraber, T.; et al. Multiscale metallic metamaterials. *Nat. Mater.* **2016**, *15*, 1100–1106. [CrossRef] [PubMed]
9. Tavoni, M.; Dapporto, M.; Tampieri, A.; Sprio, S. Bioactive Calcium Phosphate-Based Composites for Bone Regeneration. *J. Compos. Sci.* **2021**, *5*, 227. [CrossRef]
10. Gu, D. *Laser Additive Manufacturing of Metallic Materials and Components*; Elsevier: Amsterdam, The Netherlands, 2023; pp. 783–804.
11. Deshpande, V.S.; Fleck, N.A.; Ashby, M.F. Effective properties of the octet-truss lattice material. *J. Mech. Phys. Solids* **2001**, *49*, 1747–1769. [CrossRef]
12. Gibson, L.J.; Ashby, M.F. *Cellular Solids: Structure and Properties*, 2nd ed.; Cambridge University Press: Cambridge, UK, 1997.
13. Miao, X.; Hu, J.; Xu, Y.; Su, J.; Jing, Y. Review on mechanical properties of metal lattice structures. *Compos. Struct.* **2024**, *342*, 118267. [CrossRef]
14. Zhang, L.; Feih, S.; Daynes, S.; Chang, S.; Wang, M.Y.; Wei, J.; Lu, W.F. Pseudo-ductile fracture of 3D printed alumina triply periodic minimal surface structures. *J. Eur. Ceram. Soc.* **2020**, *40*, 408–416. [CrossRef]
15. Banerjee, S. On the mechanical properties of hierarchical lattices. *Mech. Mater.* **2014**, *72*, 19–32. [CrossRef]
16. Gu, D. *Laser Additive Manufacturing of High-Performance Materials*; Springer: Berlin/Heidelberg, Germany, 2015.
17. García-Hernández, C.; García-Cabezón, C.; González-Diez, F.; Ampudia, M.; Juanes-Gusano, D.; Rodriguez-Cabello, J.C.; Martín-Pedrosa, F. Effect of processing on microstructure, mechanical properties, corrosion and biocompatibility of additive manufacturing Ti-6Al-4V orthopaedic implants. *Sci. Rep.* **2025**, *15*, 14087. [CrossRef] [PubMed]
18. Thijs, L.; Verhaeghe, F.; Craeghs, T.; Humbeeck, J.V.; Kruth, J.-P. A study of the microstructural evolution during selective laser melting of Ti–6Al–4V. *Acta Mater.* **2010**, *58*, 3303–3312. [CrossRef]
19. Liu, S.; Shin, Y.C. Additive manufacturing of Ti6Al4V alloy: A review. *Mater. Des.* **2019**, *164*, 107552. [CrossRef]
20. Mirhakimi, A.s.; Dubey, D.; Elbestawi, M.A. Laser powder bed fusion of bio-inspired metamaterials for energy absorption applications: A review. *J. Mater. Res. Technol.* **2024**, *31*, 2126–2155. [CrossRef]
21. Yuan, X.; Li, G.; Zhang, L.; Song, J.; Chen, J.; Zheng, J.; Li, H.; Xie, S.; Wang, F.; Wan, Q.; et al. Spatial orientation on manufacturing fidelity and mechanical-transport-biological performances of 3D-printed microlattice structures. *Compos. Struct.* **2025**, *372*, 119551. [CrossRef]
22. Gibson, L.J.; Ashby, M.F. The Mechanics of Three-Dimensional Cellular Materials. *Proc. R. Soc. A Math.* **1982**, *382*, 43–59. [CrossRef]
23. Ashby, M.F. The properties of foams and lattices. *Philos. Trans. R. Soc. A Math. Phys. Eng. Sci.* **2005**, *364*, 15–30. [CrossRef]
24. McArthur, D.; Leung, C.L.A.; Tan, P.J. Tuning the mechanical behaviour of additively manufactured meta-materials with twinning and meta-harmonics. *Virtual Phys. Prototyp.* **2025**, *20*, e2512977. [CrossRef]

25. Zhong, H.; Song, T.; Li, C.; Das, R.; Gu, J.; Qian, M. The Gibson-Ashby model for additively manufactured metal lattice materials: Its theoretical basis, limitations and new insights from remedies. *Curr. Opin. Solid State Mater. Sci.* **2023**, *27*, 101081. [CrossRef]
26. Zhang, L.; Song, B.; Choi, S.-K.; Yao, Y.; Shi, Y. Anisotropy-inspired, simulation-guided design and 3D printing of microlattice metamaterials with tailored mechanical-transport performances. *Compos. Part B Eng.* **2022**, *236*, 109837. [CrossRef]
27. Zhang, L.; Song, B.; Zhang, J.; Yao, Y.; Lu, J.; Shi, Y. Decoupling microlattice metamaterial properties through a structural design strategy inspired by the Hall–Petch relation. *Acta Mater.* **2022**, *238*, 118214. [CrossRef]
28. White, B.C.; Garland, A.; Alberdi, R.; Boyce, B.L. Interpenetrating lattices with enhanced mechanical functionality. *Addit. Manuf.* **2021**, *38*, 101741. [CrossRef]
29. Dong, L. Mechanical response of Ti–6Al–4V hierarchical architected metamaterials. *Acta Mater.* **2019**, *175*, 90–106. [CrossRef]
30. Zhang, Z.; Song, B.; Fan, J.; Wang, X.; Wei, S.; Fang, R.; Zhang, X.; Shi, Y. Design and 3D Printing of Graded Bionic Metamaterial Inspired by Pomelo Peel for High Energy Absorption. *Chin. J. Mech. Eng. Addit. Manuf. Front.* **2023**, *2*, 100068. [CrossRef]
31. Wu, J.; Yang, F.; Li, L.; Li, P.; Xu, X.; Zhang, Y. Multi-feature bionic gradient hierarchical lattice metamaterials with multi-synergistic crushing mechanisms. *Int. J. Mech. Sci.* **2024**, *283*, 109383. [CrossRef]
32. Wang, P.; Guo, J.; Yuan, Y.; Li, C.; Wang, Y.; Guang, M.; Yan, J.; Liu, W.; Sun, Z. Bio-inspired vertex-offset lattice metamaterials with enhanced stress stability and energy absorption. *Thin-Walled Struct.* **2025**, *210*, 113060. [CrossRef]
33. Efstathiadis, A.; Symeonidou, I.; Tsongas, K.; Tzimtzimis, E.K.; Tzetzis, D. Parametric Design and Mechanical Characterization of 3D-Printed PLA Composite Biomimetic Voronoi Lattices Inspired by the Stereom of Sea Urchins. *J. Compos. Sci.* **2023**, *7*, 113. [CrossRef]
34. Wu, J.; Zhang, Y.; Yang, F.; Jiang, F.; Xu, X.; Tan, Y.; Su, L. A hybrid architectural metamaterial combing plate lattice and hollow-truss lattice with advanced mechanical performances. *Addit. Manuf.* **2023**, *76*, 103764. [CrossRef]
35. Sun, Z.; Gong, Y.; Bian, Z.; Zhang, J.; Zhao, L.; Hu, N. Mechanical properties of bionic lattice and its hybrid structures based on the microstructural design of pomelo peel. *Thin-Walled Struct.* **2024**, *198*, 111715. [CrossRef]
36. Zhang, L.; Liu, H.; Song, B.; Gu, J.; Li, L.; Shi, W.; Li, G.; Zhong, S.; Liu, H.; Wang, X.; et al. Wood-inspired metamaterial catalyst for robust and high-throughput water purification. *Nat. Commun.* **2024**, *15*, 2046. [CrossRef] [PubMed]
37. Maskery, I.; Aboulkhair, N.T.; Aremu, A.O.; Tuck, C.J.; Ashcroft, I.A.; Wildman, R.D.; Hague, R.J.M. A mechanical property evaluation of graded density Al-Si10-Mg lattice structures manufactured by selective laser melting. *Mater. Sci. Eng. A* **2016**, *670*, 264–274. [CrossRef]
38. Zhang, L.; Song, B.; Fu, J.J.; Wei, S.S.; Yang, L.; Yan, C.Z.; Li, H.; Gao, L.; Shi, Y.S. Topology-optimized lattice structures with simultaneously high stiffness and light weight fabricated by selective laser melting: Design, manufacturing and characterization. *J. Manuf. Process.* **2020**, *56*, 1166–1177. [CrossRef]
39. Waqar, S.; Hussain, S.; Ren, C.; Wang, M.; Nazir, A.; Dan, X.; Wang, C.; Chen, Z. Superior strength and energy absorption capability of LPBF metallic functionally graded lattice structures. *Thin-Walled Struct.* **2024**, *205*, 112471. [CrossRef]
40. Sun, Z.; Gong, Y.; Tian, Y.; Lang, J.; Zhang, J.; Zhao, L.; Hu, N. Design and Mechanical Properties of Layered Gradient Lattice Structures Based on Additive Manufacturing. *Addit. Manuf. Front.* **2025**, *4*, 200188. [CrossRef]
41. Yin, X.; Cui, H.; Hu, H.; Xu, H.; Yang, T. Design and mechanical characterization of novel triply periodic minimal surface-based lattice structures with high strength and energy absorption. *Compos. Struct.* **2026**, *382*, 120062. [CrossRef]
42. Xia, X.; Chen, J.; Zhang, L.; Zhong, S.; Song, J.; Yang, C.; Gao, J.; Li, G.; Wang, S.; Zhang, Z.; et al. Bambusa ventricosa-inspired strut topology for mechanical-transport-thermal performance in laser powder bed fused microlattice metamaterials. *Met. Adv.* **2026**, *45*, 25–41. [CrossRef]
43. Yang, H.; Liu, Z.; Xia, Y.; Fan, W.; Taylor, A.C.; Han, X. Mechanical properties of hierarchical lattice via strain gradient homogenization approach. *Compos. Part B Eng.* **2024**, *271*, 111153. [CrossRef]
44. Santos, J.; Sohouli, A.; Suleman, A. Micro- and Macro-Scale Topology Optimization of Multi-Material Functionally Graded Lattice Structures. *J. Compos. Sci.* **2024**, *8*, 124. [CrossRef]
45. Ge, J.; Song, Y.; Chen, Z.; Zhuo, Y.; Wei, T.; Ge, C.; Cheng, Y.; Liu, M.; Jia, Q. Effect of Geometrical Parameters on the Mechanical Performance of Bamboo-Inspired Gradient Hollow-Strut Octet Lattice Structure Fabricated by Additive Manufacturing. *Micromachines* **2024**, *15*, 583. [CrossRef] [PubMed]
46. Ali, D.; Sen, S. Finite element analysis of mechanical behavior, permeability and fluid induced wall shear stress of high porosity scaffolds with gyroid and lattice-based architectures. *J. Mech. Behav. Biomed. Mater.* **2017**, *75*, 262–270. [CrossRef] [PubMed]
47. Ali, D. Effect of scaffold architecture on cell seeding efficiency: A discrete phase model CFD analysis. *Comput. Biol. Med.* **2019**, *109*, 62–69. [CrossRef] [PubMed]
48. Nhaichaniya, G.K.; Kumar, M.; Dayal, R. Improvement in Active Cell Proliferation Area at Higher Permeability With Novel TPMS Lattice Structure. *J. Biomech. Eng.* **2024**, *146*, 111009. [CrossRef] [PubMed]
49. Castro, A.P.G.; Pires, T.; Santos, J.E.; Gouveia, B.P.; Fernandes, P.R. Permeability versus Design in TPMS Scaffolds. *Materials* **2019**, *12*, 1313. [CrossRef] [PubMed]

50. Bocharov, G.S.; Dedov, A.V.; Eletskii, A.V.; Vagin, A.O.; Zacharenkov, A.V.; Zverev, M.A. Thermal Balance of a Water Thermal Accumulator Based on Phase Change Materials. *J. Compos. Sci.* **2023**, *7*, 399. [CrossRef]
51. Maskery, I.; Aremu, A.O.; Parry, L.; Wildman, R.D.; Tuck, C.J.; Ashcroft, I.A. Effective design and simulation of surface-based lattice structures featuring volume fraction and cell type grading. *Mater. Des.* **2018**, *155*, 220–232. [CrossRef]
52. Zheng, X.; Fu, Z.; Du, K.; Wang, C.; Yi, Y. Minimal surface designs for porous materials: From microstructures to mechanical properties. *J. Mater. Sci.* **2018**, *53*, 10194–10208. [CrossRef]
53. He, X.; Li, G.; Zhang, L.; Huang, Y.; Xie, B.; Shi, Z.; Feng, G.; Liu, W.; Lyu, F.; Wang, S.; et al. Bio-inspired material-structure-function integrated additive manufacturing of Al-based metamaterials with surpassing energy absorption. *Sci. Adv.* **2025**, *11*, eaea0430. [CrossRef] [PubMed]
54. Hao, B.; Zhu, Z.; Zhang, L. Network-based and sheet-based Gyroid lattice structures with different gradient directions: Manufacture, mechanical response and energy absorption. *Meccanica* **2024**, *59*, 1911–1926. [CrossRef]
55. *ISO 13314:2011*; Mechanical Testing of Metals—Ductility Testing—Compression Test for Porous and Cellular Metals. ISO: Geneva, Switzerland, 2011.
56. Xue, X.; Patel, M.K.; Kersaudy-Kerhoas, M.; Desmulliez, M.P.Y.; Bailey, C.; Topham, D. Analysis of fluid separation in microfluidic T-channels. *Appl. Math. Model.* **2012**, *36*, 743–755. [CrossRef]
57. Bartnikowski, M.; Klein, T.; Melchels, F.; Woodruff, M. Effects of scaffold architecture on mechanical characteristics and osteoblast response to static and perfusion bioreactor cultures. *Biotechnol. Bioeng.* **2014**, *111*, 1440–1451. [CrossRef] [PubMed]

Disclaimer/Publisher's Note: The statements, opinions and data contained in all publications are solely those of the individual author(s) and contributor(s) and not of MDPI and/or the editor(s). MDPI and/or the editor(s) disclaim responsibility for any injury to people or property resulting from any ideas, methods, instructions or products referred to in the content.